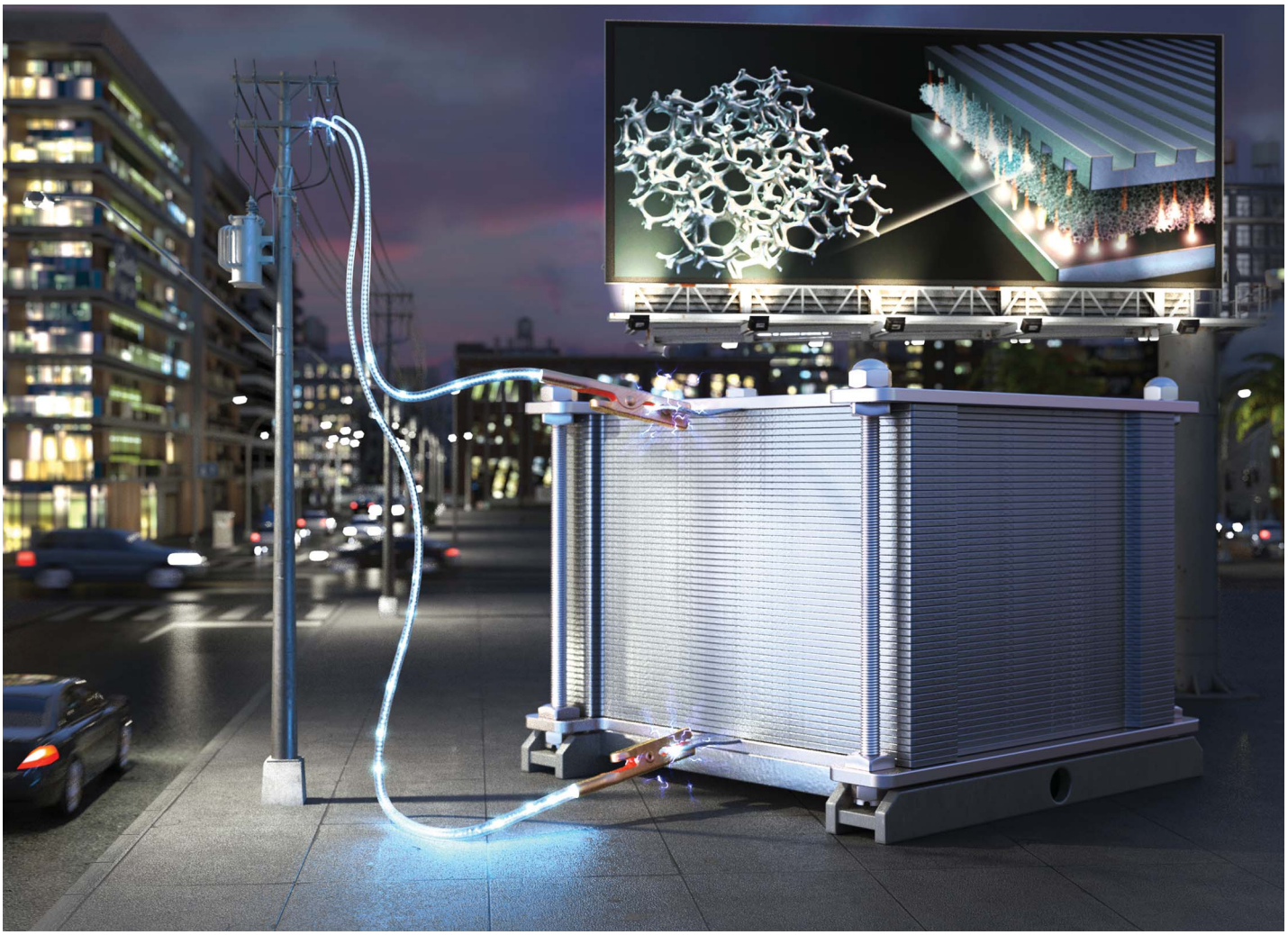

Highlighting a study on a high-temperature current collector for solid oxide fuel cells by Dr Kyung Joong Yoon's group from Korea Institute of Science and Technology and Dr Insung Lee's group from E&KOA.

Construction of high-temperature electronic conduction paths for the scale-up of solid oxide fuel cell technology

We report a Cu–Mn foam as a highly efficient, reliable, and cost-competitive current collector for solid oxide fuel cells. The metallic alloy foam transforms into a conductive spinel oxide at high temperatures, providing desirable electrical properties. It is incorporated into a 1 kW stack and demonstrates excellent performance and durability.

As featured in:

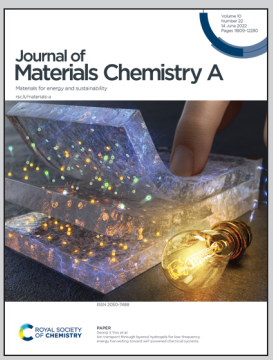

See Insung Lee, Kyung Joong Yoon *et al.*, *J. Mater. Chem. A*, 2022, **10**, 11917.

ROYAL SOCIETY OF CHEMISTRY

rsc.li/materials-a

Registered charity number: 207890

Journal of Materials Chemistry A

ROYAL SOCIETY OF CHEMISTRY

PAPER

View Article Online
View Journal | View Issue

Cite this: J. Mater. Chem. A, 2022, 10, 11917

Construction of high-temperature electronic conduction paths for the scale-up of solid oxide fuel cell technology†

Mi Young Park,[ab] Sun-Young Park,[c] Haewon Seo,[a] Jin-Mook Jung,[d] Hyo Ki Hwang,[d] Jongsup Hong,[ef] Jun-Young Park,[g] Insung Lee *[d] and Kyung Joong Yoon *[af]

Received 28th March 2022
Accepted 5th May 2022

DOI: 10.1039/d2ta02468c

rsc.li/materials-a

Solid oxide fuel cells (SOFCs) currently face great opportunities in various applications. One of the critical issues for their commercialization involves cathode current collection in full-scale stacks because forming a reliable electronic conduction path in high-temperature oxidizing environments is extremely difficult. Herein, we present a Cu–Mn foam as a highly efficient, reliable, and cost-competitive cathode current collector. The Cu–Mn foam exists as a metallic alloy in the as-fabricated state, which offers adequate mechanical properties for stack assembly. Subsequently, it transforms into a conductive spinel oxide during high-temperature operation, providing the desired electrical and structural characteristics. Resistance measurements at 700 °C verify that the Cu–Mn foam was stable for 27 000 h. In unit cell testing, the foam performs comparably to a noble metal (Pt) mesh, and when the cell is enlarged from 4 to 100 cm^2, no performance loss occurs. Furthermore, it is successfully incorporated into a 1 kW-class full-size stack, where it demonstrates excellent durability in accelerated tests involving thermal and current cycling for 3684 h. This developed Cu–Mn foam can overcome a crucial limitation in the scale-up of SOFC technology and can also be utilized to construct high-temperature electronic conduction paths in various applications.

1. Introduction

Solid oxide fuel cells (SOFCs) offer one of the most efficient, versatile, and environmentally friendly means of converting the chemical energy of fuel into electrical power.[1–3] Thanks to their unique advantages over conventional power generation systems, SOFCs have been extensively investigated over the last several decades, and remarkable technical advances have been achieved, particularly their significantly improved cell performance. In the early stages of SOFC development, cathode-supported tubular and electrolyte-supported planar designs were most commonly pursued owing to their ease of sealing and simple manufacturing processes,[4,5] but they inherently possess high internal resistance and exhibit low power densities. In the late 1990s, an anode-supported planar design with a thin electrolyte was developed, which drastically improved performance. For instance, an anode-supported cell with a 10 μm-thick electrolyte enabled a maximum power density close to ~2 W cm^{-2} at 800 °C.[6,7] Since then, the development of new active materials and nanostructured components has further enhanced the performance, and extremely high power densities of over 3 W cm^{-2} have been achieved using standard 8 mol% yttria-stabilized zirconia (YSZ) electrolyte in recent years.[8,9] As a result, SOFC technology has demonstrated superior characteristics over conventional power generation systems and is facing great opportunities in a broad range of applications. Currently, the remaining issues hindering its successful commercialization include the implementation of such advanced cell technologies in practical full-scale stacks. In SOFC systems, multiple cells are integrated into stacks to attain the desired power output, and the typical area of each cell is ~100 cm^2. In general, the cell performance is substantially degraded by enlarging the cell area and assembling it into stacks.[10–12] A major source of such performance loss is the electrical contact between the cell and interconnect rather than the cell itself.[10,13–15] Improving this interfacial contact can decrease the overall resistance by more than 70%,[16] and

[a]High-Temperature Energy Materials Research Center, Korea Institute of Science and Technology, Seoul, Korea. E-mail: lance@enkoa.co.kr
[b]Department of Materials Science and Engineering, Korea University, Seoul, Korea
[c]Technological Convergence Center, Korea Institute of Science and Technology, Seoul, Korea
[d]E&KOA, Daejeon, Korea
[e]School of Mechanical Engineering, Yonsei University, Seoul, Korea
[f]Yonsei-KIST Convergence Research Institute, Seoul, Korea
[g]HMC, Department of Nanotechnology and Advanced Materials Engineering, Sejong University, Seoul, Korea

† Electronic supplementary information (ESI) available. See https://doi.org/10.1039/d2ta02468c

accordingly, extensive research efforts have been devoted to lowering the contact resistance.[10,15,17,18]

The formation of uniform electrical conduction paths between the cell and interconnect is significantly more demanding for the cathode side than for the anode side.[19,20] For the anode side, which is supplied with H_2, nickel mesh or foam is widely used because metallic nickel is highly conductive and stable in a reducing atmosphere at high temperatures. In contrast, air is supplied to the cathode side, and few materials exhibit adequate electrical conductivity and stability in an oxidizing atmosphere at high temperatures. In lab-scale experiments, noble metals, such as Pt, Au, and Ag, are often used to minimize contact resistance,[13,17,21] but their high costs make them unsuitable for industrial use. Applying a conductive ceramic layer has been considered as a practical approach.[22–25] Although this thin ceramic contact layer lowers the interfacial resistance to a certain degree, it does not provide structural compliance to accommodate the geometric irregularities between the two rigid components over a large area. The contact formed by the thin layer is particularly vulnerable when the cells and interconnects structurally deform during thermal cycling. A stainless steel mesh with a protective ceramic coating has been proposed as a cathode current collector,[26,27] but the brittleness of this coating risks exposing the stainless steel to hot air, which causes rapid oxidation and Cr evaporation. Ceramic foams have also been evaluated[28] but were found to be impractical owing to their brittleness and handling difficulties. In summary, most existing measures have inherent limitations, and very few novel approaches have functioned properly in realistic stacks. Hence, a technical breakthrough is urgently required for the successful scale-up and commercialization of SOFC technology.

In this study, we developed a Cu–Mn foam that fulfills all the strict requirements mentioned above in practical SOFC stacks. At room temperature, the Cu–Mn foam exists as a metallic alloy that provides adequate mechanical strength and ductility for handling during stack assembly. Then, during operation at high temperatures, it transforms into a highly conductive spinel oxide, thereby forming effective conduction paths between the cell and interconnect in an oxidizing atmosphere. The foam offers compliance between the two rigid components and accommodates geometric variations to maintain contact during severe changes in the temperature and electrical load. The reliability of the Cu–Mn foam was verified in a 1 kW stack *via* long-term operation over 3000 h.

2. Experimental

To prepare Cu–Mn foam, commercial Cu foam was used as a skeleton, and Mn-rich Cu–Mn oxide powder (80 wt% Mn–20 wt% Cu) was deposited on Cu foam by electrostatic powder coating. The electrostatic powder coating process is typically used to deposit ceramic power on a metal substrate. During the coating process, the Cu–Mn spinel powder was charged by an electric field created by a corona spray gun and sprayed onto the Cu foam. After deposition, the foam was thermally treated at 850 °C in a H_2 atmosphere for 1 h to yield a metallic Cu–Mn alloy. The amount of deposited Cu–Mn oxide powder was adjusted to yield an overall composition of 40 wt% Cu–60 wt% Mn. X-ray diffraction (XRD) patterns were recorded with a Rigaku D/max-2500 employing a nickel-filtered Cu Kα radiation source. The microstructure of the foam was investigated using optical microscopy and scanning electron microscopy (SEM) (Inspect-F, FEI). Finally, the composition was determined using energy-dispersive X-ray spectroscopy (EDS) and EPMA.

To examine the electrical properties, the area specific resistance (ASR) of the Cu–Mn foam was measured. A sample with dimensions of 1 cm × 1 cm was placed between two stainless steel interconnect (SS460FC developed by POSCO, Republic of Korea) blocks, and two Pt wires were welded to the outer surface of each block for electrical measurements. The Cu–Mn foam and interconnect blocks were placed between two alumina plates, and pressure was applied by tightening four bolts connecting the plates. Mica sheets were inserted between the blocks and plates to evenly distribute the applied pressure, which was controlled using a torque wrench. ASR was measured using the four-probe method. A schematic of the ASR measurement setup is displayed in Fig. S1 in the ESI.† The ASR data were collected at 700 °C in air for 21 000 h.

Unit cells were tested using two types of commercial cells purchased from Elcogen. The cells consisted of a Ni–YSZ anode support (~370 μm), a Ni–YSZ anode functional layer (~10 μm), a YSZ electrolyte (~3 μm), a gadolinium-doped ceria (GDC) diffusion barrier layer (~2 μm), and LSC-GDC cathode (~12 μm). The areas of the tested cells were 2 cm × 2 cm (effective electrode area: 1 cm^2) and 10 cm × 10 cm (effective electrode area: 81 cm^2). The cells were tested in a one-cell stack configuration comprising the cells, interconnects, sealants, and current collectors. The cell was placed between two interconnects made of Crofer 22 APU, and the cells were sealed with a glass-ceramic sealant that is composed of 60 wt% Pyrex glass and 40 wt% α-Al_2O_3 particulates. Either Cu–Mn foam or Pt mesh was placed between the cell cathode and the interconnect for current collection. The Cu–Mn foam used for cell testing was ~300 μm-thick and 80–90% porous. Its cell size was 300–500 μm and strut thickness was 60–80 μm. For Pt mesh, the wire diameter was 0.06 mm and open area was 65%. The nominal aperture was 0.25 mm and thickness was 0.12 mm. On the anode side, Ni foam was inserted between the cell and interconnect. Fig. S2† shows a schematic of the unit cell test setup. The assembled test setup was placed in a furnace and heat-treated under a mechanical load at 850 °C for 5 h to form a tight seal. Then, humidified hydrogen (3% H_2O) and air were supplied to the anode and cathode, respectively. After the NiO in the anode was completely reduced to metallic Ni, the cell was electrochemically characterized at 650–750 °C using a Scribner 890C Fuel Cell Test System and a Solarton 1260/1287 potentiostat-frequency response analyzer.

A 1 kW-class stack incorporating the Cu–Mn foam was also fabricated and evaluated at E&KOA. The stack was composed of 30 anode-supported cells (12 cm × 12 cm) purchased from Elcogen, glass-ceramic sealants, stainless-steel interconnects (SS460FC), a Cu–Mn foam cathode current collector, and a Ni foam anode current collector. The stack employed internal manifolds and cross-flow channel design. The sealants were

applied using slurry dispensing equipment. After conditioning at 700 °C, the power generation characteristics were evaluated up to a total current of 43 A. Subsequently, to test the stack's durability, it was operated for 3864 h, including six thermal cycles, 52 load cycles, and 57 load trips. The temperature was cycled between 25 °C and 700 °C at heating and cooling rates of 1 °C min^{-1}. During the load cycling, the electric load was varied between 120 and 200 mA cm^{-2} at a rate of 2 mA cm^{-2} min^{-1}. During the load trips, the electric load was abruptly turned on and off between 0 and 200 mA cm^{-2}. During static operation, the current density was maintained at 200 mA cm^{-2}. After operation, the stack was cooled and disassembled for post-mortem analysis, and the Cu–Mn foam tested in the stack was analyzed using SEM.

3. Results and discussion

Cu–Mn spinel oxides can be formed by the oxidation of binary metallic alloys, and they provide high electrical conductivity at high temperatures in an oxidizing atmosphere. Spinel oxides consist of a close-packed oxygen lattice with cations in tetrahedral and octahedral positions. The most stable configuration for Cu–Mn spinel, is known to contain tetrahedral Cu^{+} and octahedral Mn^{4+},[29] and this spinel exhibits higher electrical conductivity than most other spinel materials owing to the large oxygen gap between the crystals.[20] Specifically, the electrical conductivity of $Cu_{1.3}Mn_{1.7}O_4$ was reported to be as high as 225 S cm^{-1} at 750 °C.[30] For the electrical connection between the cell and interconnect in SOFC stacks, foam is considered to be the most favorable structure because it provides sufficient porosity and structural compliance, and its moderate solid fraction provides a good balance of contact area and gas flow.[28,31] In this study, we fabricated a Cu–Mn metallic alloy foam that transforms into a spinel oxide at high temperatures in SOFC stacks during operation. To fabricate the Cu–Mn metallic alloy foam, commercial Cu foam was used as the backbone, and a Mn-rich Cu–Mn spinel powder (80 wt% Mn–20 wt% Cu) was deposited onto both its outer surface and the inner pore surfaces by electrostatic powder coating. During the coating process, the Cu–Mn spinel powder was charged by an electric field created by a corona spray gun and sprayed onto the Cu foam. The electrostatic attractive force between the charged Cu–Mn spinel powder and Cu foam leads to particle deposition, whereas the repulsive force between the charged particles prevents severe agglomeration, thereby enabling uniform powder deposition. During this process, the overall composition of the Cu–Mn alloy was controlled by adjusting the amount of deposited particles. The target composition was 40 wt% Cu–60 wt% Mn. After deposition, the foam was thermally treated in a reducing atmosphere to yield a metallic Cu–Mn alloy.

The structural characteristics of the Cu–Mn foam are presented in Fig. 1. The photograph of the as-fabricated Cu–Mn foam in Fig. 1(a) confirms its sufficient mechanical strength and flexibility in the metallic alloy state, *i.e.*, no difficulties in handling or risk of breakage arise during stack assembly. The optical microscopy image in Fig. 1(b) exhibits a homogeneous

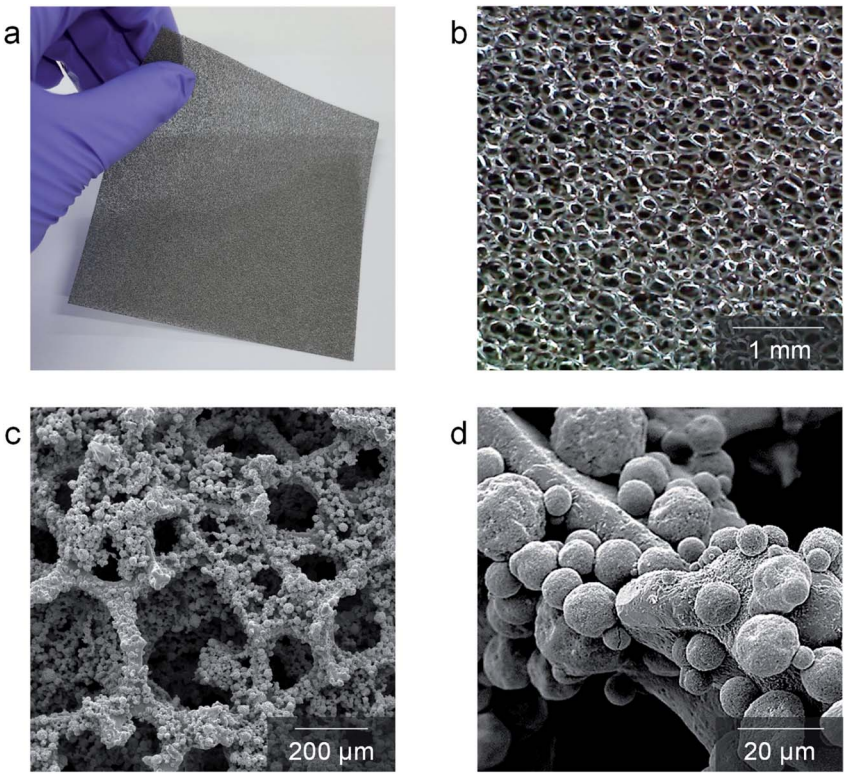

Fig. 1 Structural characteristics of Cu–Mn foam: (a) photograph and (b) optical microscope images of as-fabricated Cu–Mn foam. (c and d) SEM images of Cu–Mn foam in (c) low- and (d) high-magnifications.

open-cell structure with a three-dimensionally connected solid phase and interconnected pores, which provide continuous paths for both electrical conduction and gas transport, respectively. In SEM image of the as-fabricated Cu–Mn foam in Fig. 1(c), the cell size is in the range of 300–500 μm, and the electrostatically deposited particles uniformly coat all surfaces. Based on the magnified SEM image in Fig. 1(d), the particle size is in the range of 10–20 μm. After heat-treatment at 800 °C for 2 h, the volume of the foam and particles clearly expanded, as shown in Fig. S3,† owing to the oxidation of the metallic Cu–Mn alloy to spinel oxide. The strut thickness was ~40–60 μm in the metallic alloy state and increased to ~60–80 μm after oxidation. The modulus of the foam correlates with strut thickness,[32,33] and such thick struts are expected to provide sufficient mechanical strength during stack assembly and operation. In addition, the morphological features smoothed after oxidation, and the boundaries between the particles and backbone were less sharp. Such morphological changes may have been caused by high-temperature interdiffusion, which may have homogenized the composition. The porosity of the foam before and

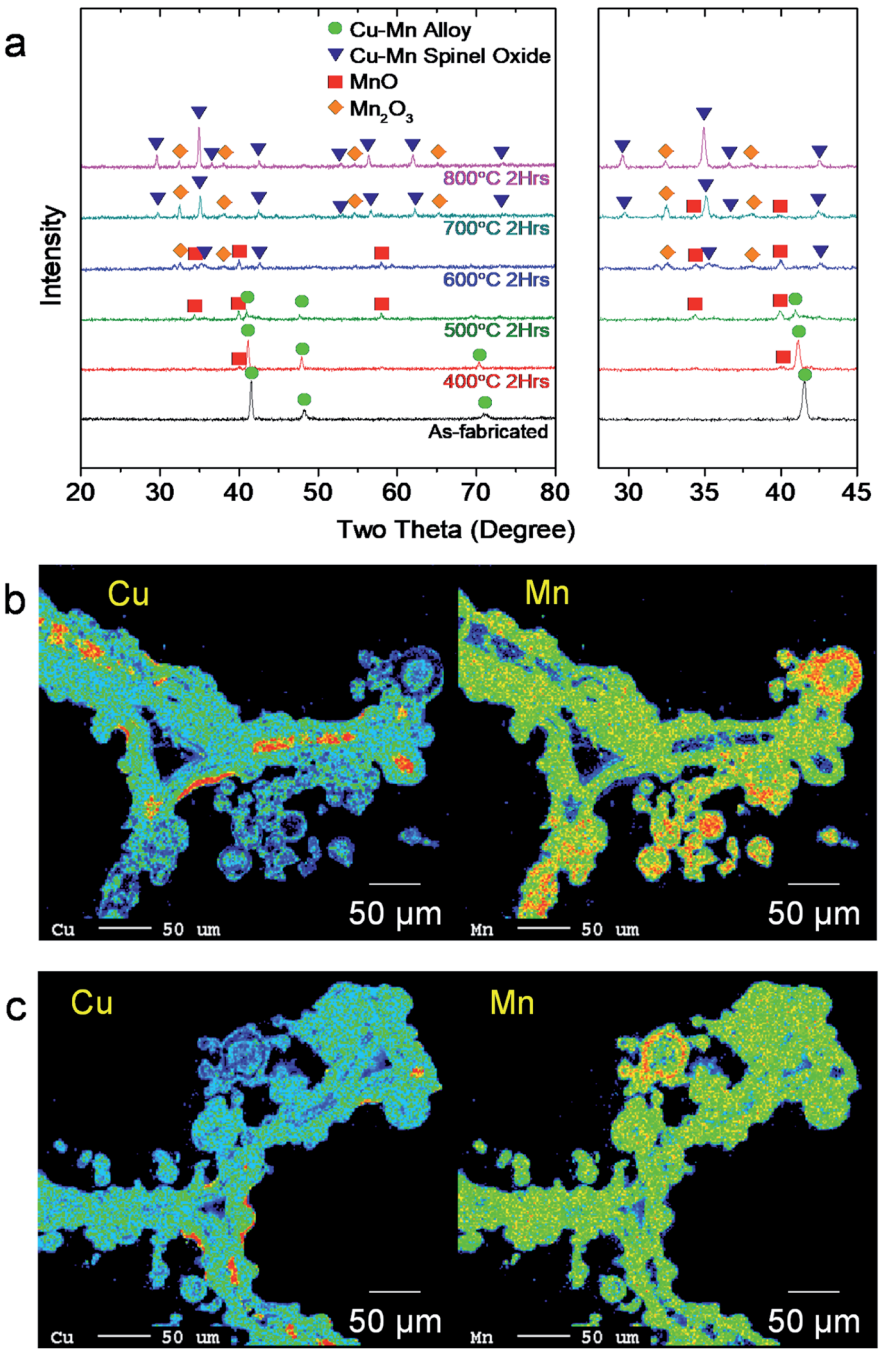

Fig. 2 Chemical characteristics of Cu–Mn foam: (a) XRD patterns of as-fabricated and thermally treated (400–800 °C for 2 h) Cu–Mn foams. (b and c) EPMA elemental analysis of Cu–Mn foam in the (b) as-fabricated state and (c) after heat-treatment at 800 °C for 2 h.

after oxidation was estimated to be ~90% and ~80%, respectively, through an image analysis (Fig. S4†). The relative density and porosity of the foam can also be assessed by a dimensional analysis,[34,35] and the solid fraction, ρ, is related to the strut geometry as[33]

$$\rho \propto \left(\frac{t}{l}\right)^2 \quad (1)$$

where t and l denote the strut thickness and length, respectively. The average length of the struts shown in Fig. 1(c) and (d) was estimated to be ~150 μm, which is reasonably consistent with the results of the image analysis, *i.e.*, the solid struts account for ~11% and ~21% of the sample volume before and after oxidation, corresponding to porosities of ~89% and ~79%, respectively. Such high porosity allows facile gas transport, as confirmed by permeability measurements in Fig. S5.†

The chemical properties of the Cu–Mn foam are presented in Fig. 2. The XRD analysis in Fig. 2(a) shows the phase evolution of the Cu–Mn foam upon heating from room temperature to 800 °C. In this experiment, the XRD patterns of Cu–Mn foam were collected from the as-fabricated state and after heat-treatments at 400–800 °C for 2 h in air. The as-fabricated Cu–Mn foam exists as a metallic Cu–Mn alloy with a face-centered cubic (FCC) structure. Indeed, Cu–Mn alloys show a wide domain of γ solid solutions in the phase diagram.[36] Upon heating, the Cu–Mn foam thermally oxidizes. For alloy systems, a single component often selectively oxidizes in the initial stage.[37,38] Thermodynamically speaking, the Mn in Cu–Mn alloys reacts with oxygen more readily than Cu, initially leading to preferential oxidation and surface enrichment of Mn.[37] After heat treatment 400–500 °C, small MnO peaks appear in the XRD pattern, along with a decrease in the Cu–Mn metal alloy peak intensities. The Cu–Mn spinel oxide peaks appear at 600 °C, and the Cu–Mn spinel oxide becomes the predominant phase, with a small amount of residual Mn_2O_3 phase at 700 °C and above. The elemental mapping results of the electron probe micro-analysis (EPMA) in Fig. 2(b) reveal compositional inhomogeneity in the as-fabricated state. Specifically, Mn-rich particles are attached to the surface of the Cu-rich backbone. After thermal treatment at 800 °C, the elemental distribution becomes more uniform, but small Mn-rich regions remain for the deposited particles (Fig. 2(c)), which is reasonably consistent with the XRD analysis in Fig. 2(a). Based on the EPMA quantitative analysis, the composition of the sample heat-treated at 800 °C was estimated to be 36–42 at% Cu and 58–64 at% Mn. Cu–Mn spinel is stable in a wide range of non-stoichiometry,[29] thus minimizing the amount of this secondary Mn-rich phase.

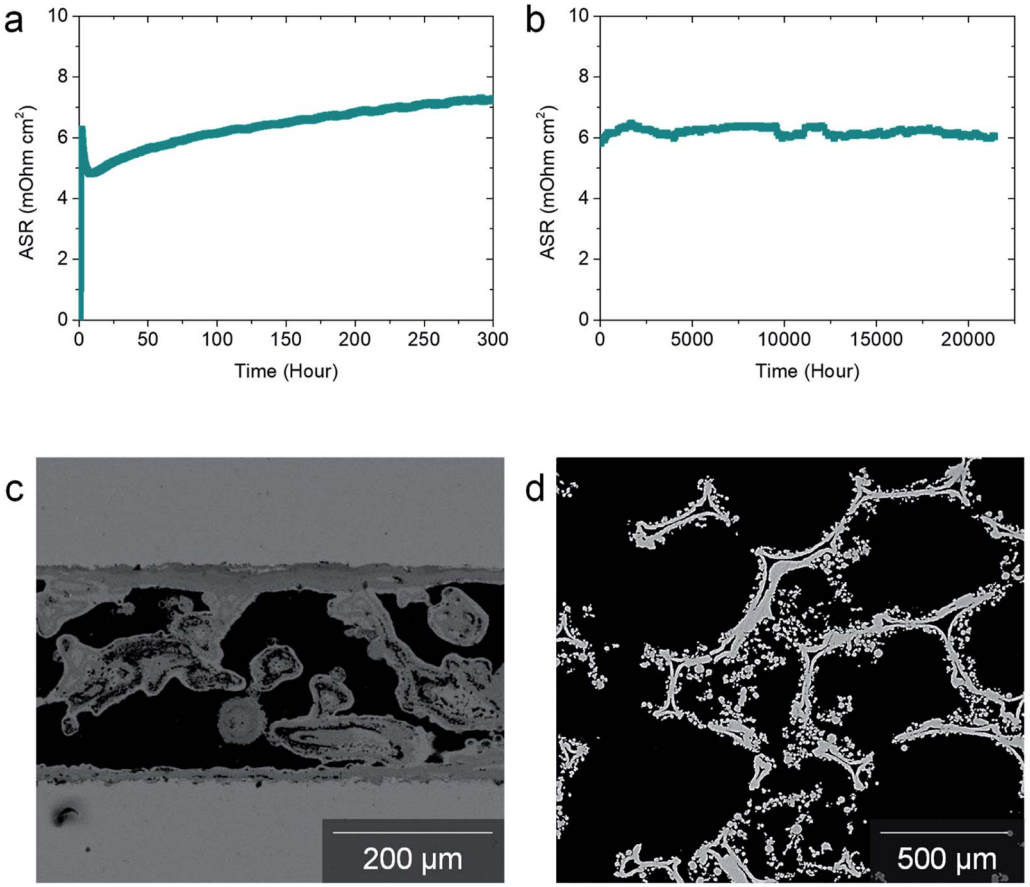

Fig. 3 High-temperature electrical properties of Cu–Mn foam: (a and b) ASR results measured for (a) initial 300 h and (b) 22 000 h at 700 °C in air. (c and d) SEM images of Cu–Mn foam after ASR measurements in (c) vertical and (d) lateral directions.

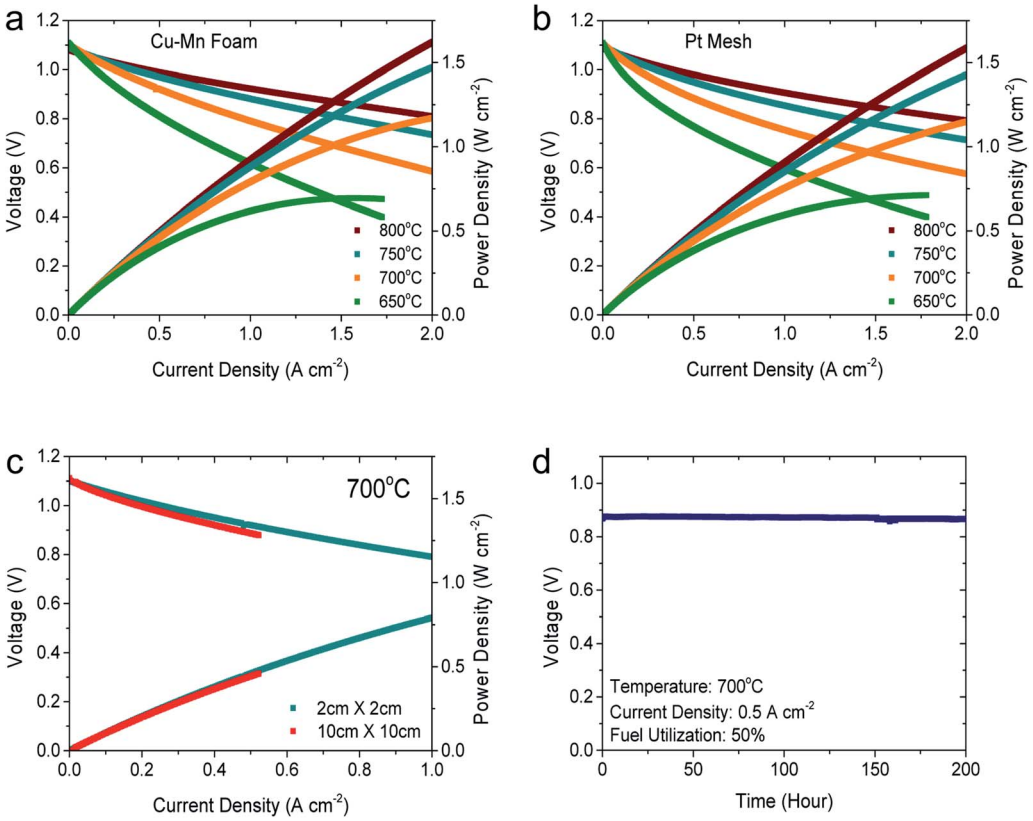

Fig. 4 Unit-cell test results: (a and b) Button cells (2 cm × 2 cm) measured at 650–800 °C using (a) Cu–Mn foam and (b) Pt mesh. (c) Performance comparison of a button cell (2 cm × 2 cm) and a large cell (10 cm × 10 cm) with Cu–Mn foams at 700 °C. (d) Long-term test results of the large cell (10 cm × 10 cm) with Cu–Mn foam at 0.5 A cm^{-2} and 700 °C.

The high-temperature electrical properties of the Cu–Mn foam were evaluated using ASR measurements. Fig. 3(a) shows the ASR data measured during the initial 300 h at 700 °C. The ASR rapidly increases during heating as the metallic Cu–Mn alloy thermally oxidizes. The ASR reaches its maximum value when the metallic phase disappears, and various poorly conductive oxide phases coexist. Subsequently, the ASR value decreases and stabilizes upon the formation of the conductive Cu–Mn spinel oxide phase. This electrical behavior of the Cu–Mn foam is closely related to the phase evolution presented in the XRD analysis in Fig. 2(a). After stabilization, the ASR gradually increases, possibly owing to the growth of oxide scale on the stainless steel interconnects used in the ASR measurements rather than a change in the Cu–Mn foam itself (Fig. S1†). Fig. 3(b) shows the ASR data measured for 21 000 h, which corresponds to 2 years and 5 months. In Fig. 3(a), the ASR gradually increases for the first ~1500 h and then remains nearly constant at ~6 mΩ cm^2 for the remaining 19 500 h, which corroborates the excellent chemical and mechanical stability of the Cu–Mn foam under SOFC operating conditions. Fig. 3(c) shows a cross-sectional SEM image of the Cu–Mn foam sandwiched between the stainless-steel interconnects used for the ASR measurements. The Cu–Mn foam provides well-connected current paths between the two interconnects and sufficient porosity for facile gas transport. The contacts between the Cu–Mn foam and the interconnects are intact, and there is no indication of structural flaws. An SEM image of the Cu–Mn foam in the lateral direction is shown in Fig. 3(d). The area fraction of electrical contact was estimated to be ~22% by an image analysis, which is substantially higher than that of the typical current collectors based on woven meshes. The typical contact area of mesh is typically in the range of 4–8%.[13,39] Moreover, the optimum fraction of contact area between the cathode and interconnect is known to be ~20%, which is very close to that of Cu–Mn foam, because lower and higher fractions cause current shrinkage and hinder gas diffusion, respectively.[20]

To evaluate its feasibility in practical applications, Cu–Mn foam was tested as a cathode current collector in unit cells. Fig. 4(a) and (b) compare the *I–V* curves and corresponding power densities of two identical button cells (2 cm × 2 cm) tested using the Cu–Mn foam and Pt mesh, respectively, as the cathode current collectors. A cross-sectional SEM image of the cell is displayed in Fig. S6.† The electrochemical measurements were performed at 650–800 °C with humidified H_2 (3% H_2O) as the fuel and air as the oxidant. The open-circuit voltages of the two cells, one with the Pt mesh and the other with the Cu–Mn foam, were close to the theoretical values, indicating that the cells and seals were leak-tight. The *I–V* curves of the two cells in Fig. 4(a) and (b) are very similar, and Table 1 confirms nearly identical power densities of the two cells at 0.7 V. Moreover, the impedance spectra of the two cells are similar with nearly identical

Table 1 Power densities of the cells tested with Cu–Mn foam and Pt mesh at 0.7 V and 650–800 °C. Humidified H_2 (3% H_2O) and air were supplied to the anode and cathode, respectively, at a flow rate of 200 sccm

	Power density (W cm^{-2}) at 0.7 V	
Temperature (°C)	Cu–Mn foam	Pt mesh
800	2.05	2.11
750	1.57	1.48
700	0.99	0.88
650	0.54	0.47

ohmic and polarization resistances in Fig. S7.† The contact between the electrode and interconnect determines the current distribution within the cell and strongly affects both the ohmic resistance and electrode polarization.[13] The similar performance of the two cells confirms that the Cu–Mn foam and Pt mesh offer comparable electrical contact resistance and gas permeation capabilities. Although the electrical conductivity of the Cu–Mn spinel is intrinsically lower than that of Pt, the structural advantages of the foam over the mesh, such as the large number of fine contact points and well-connected current paths, are considered to compensate for this lower conductivity, resulting in comparable overall cell performance. The similar performance in Fig. 4(a) and (b) suggests that replacing precious metals with

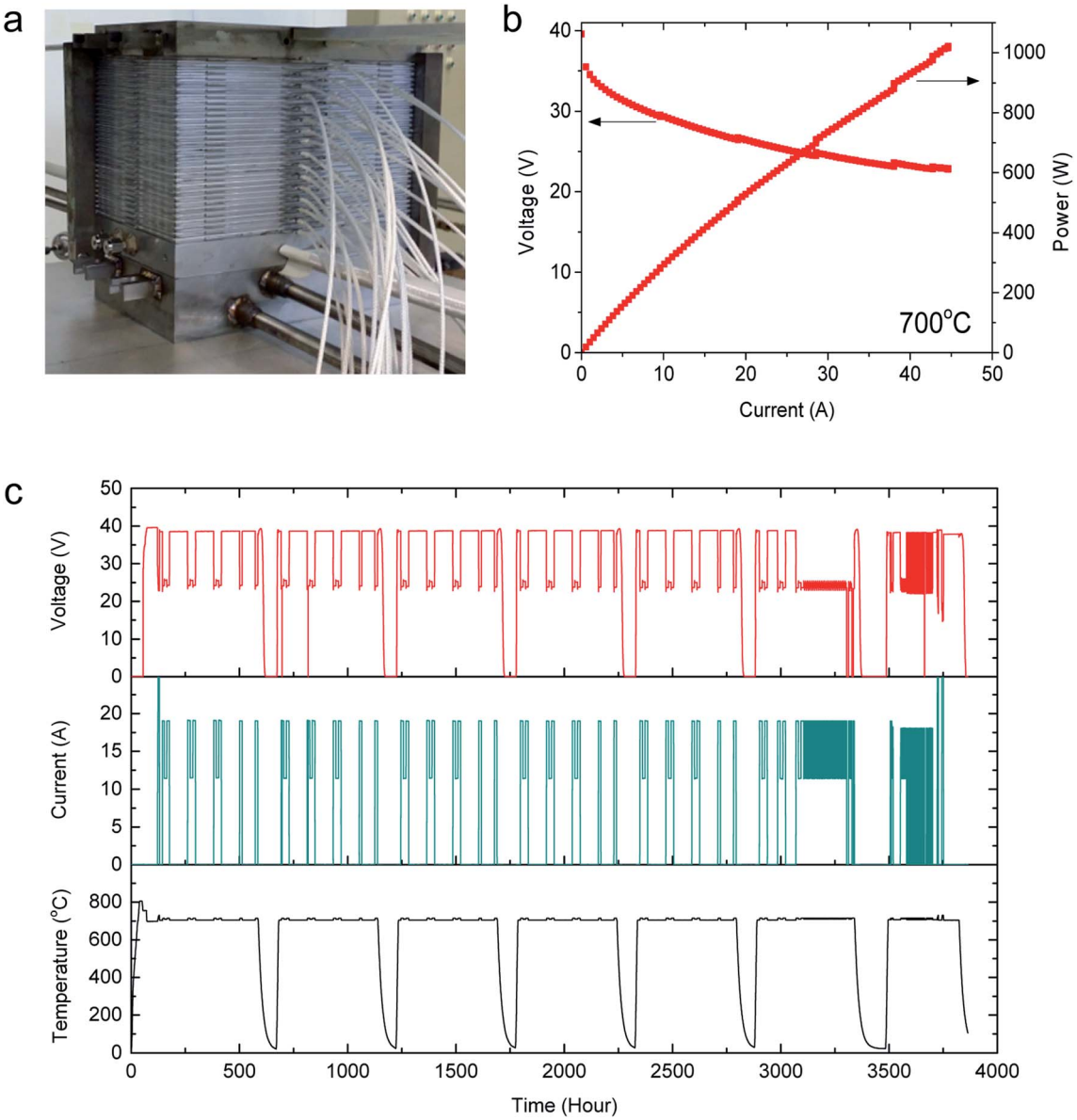

Fig. 5 Stack test results: (a) photograph of the 1 kW stack used to evaluate the Cu–Mn foams. (b) Current, voltage, and power of the stack as a function of time obtained in the initial performance evaluation, and (c) voltage, current and temperature of the stack in dynamic durability tests.

Cu–Mn foam can significantly decrease material costs without sacrificing functionality. Because the effects of contact resistance become more critical with the increasing cell size, a large cell (10 cm × 10 cm) was also tested using the Cu–Mn foam, and its performance at 700 °C was compared with that of the button cell in Fig. 4(c). The two cells show nearly identical *I–V* characteristics, indicating that the Cu–Mn foam forms a uniform electrical contact over a large area. To test its stability, this large cell with Cu–Mn foam was operated at a constant current density of 0.5 A cm^{-2} with a fuel utilization of 50% for 200 h at 700 °C. The performance degraded negligibly, suggesting that the Cu–Mn foam is chemically and structurally stable in realistic SOFC operating conditions.

Finally, the Cu–Mn foams were evaluated in a 1 kW-class stack composed of 30 anode-supported cells (12 cm × 12 cm), stainless-steel interconnects, glass-ceramic sealants, Cu–Mn foam cathode current collectors, and Ni foam anode current collectors. A photograph of the assembled stack is displayed in Fig. 5(a). Fig. 5(b) shows the *I–V* curve of the stack measured at 700 °C, wherein the stack output power reaches 1 kW at a current of 43 A. The stability of the stack was evaluated for 3684 h. As an accelerated test for the Cu–Mn foam, the stack was operated under severe dynamic changes in the electric current and temperature. The interfacial contact between the cathode of the cell and the interconnect is known to be the critical factor determining whether the stack can endure thermal and load cycles.[20] Severe damage to the contacts, such as debonding and cracks, has often been observed after dynamic operation.[40–42] In this study, the stack underwent six thermal cycles, 52 load cycles, and 57 load trips during the testing period. The thermal cycling was conducted between 700 °C and room temperature, and the load cycles were performed between 120 and 200 mA cm^{-2} at a scan rate of 2 mA cm^{-2} min^{-1}. A load trip refers to abruptly turning the electric current on and off, *i.e.*, between 0 and 200 mA cm^{-2}. As shown in Fig. 5(c), the stack exhibited excellent stability throughout the entire operation for 3684 h, and its degradation rate was measured to be 0.7% kh^{-1}. Because the durability of a stack is strongly affected by the electrical contacts under changes in temperature and electric current, the cycling test results demonstrate that the Cu–Mn foam provided stable conduction paths throughout the severe dynamic conditions. The SEM image of the Cu–Mn foam used for stack testing in Fig. S7† reveals no indication of structural changes or mechanical damage, confirming that the Cu–Mn foam can tolerate the dynamic variations in the electric load and temperature encountered during real stack operation. In addition, no compositional change was observed in EPMA elemental analysis after stack testing (Fig. S8†), indicating that Cu–Mn foam is chemically stable in SOFC operating conditions. Based on the performance, stability, and cost, the Cu–Mn foam presented in this study is expected to resolve the major issues associated with the scale-up of SOFC technology.

4. Conclusions

With rapid advances in cell technologies, cathode current collection in SOFC stacks has emerged as a critical factor in their successful commercialization. To date, numerous approaches have been proposed to form reliable conduction paths in a high-temperature oxidizing atmosphere, but most of them exhibit inherent limitations. The Cu–Mn foam presented in this study resolves the issues of existing techniques in terms of electrical, structural, thermochemical, and thermomechanical properties, as well as material costs. It is composed of 40 wt% Cu–60 wt% Mn and provides high electrical conductivity (~200 S cm^{-1}) as well as sufficient porosity (80–90%). The cell and stack evaluations demonstrated excellent performance and stability under severe SOFC operating conditions. In particular, its feasibility was verified in a realistically sized 1 kW stack, proving that it can be immediately used in practical applications. The functionality of the Cu–Mn foam can be further improved by modifying its composition and structure. Moreover, the innovative *in situ* phase transformation of the metallic foam into a conductive ceramic can be utilized in various applications requiring electric contacts in high-temperature oxidizing environments.

Conflicts of interest

There is no conflicts to declare.

Acknowledgements

This research was financially supported by the Korea Institute of Energy Technology Evaluation and Planning (KETEP) of the Ministry of Trade, Industry & Energy, Republic of Korea through the Energy Technology Development Program (No. 20203010030020). It was also partly supported by the Institutional Research Program of the Korea Institute of Science and Technology (KIST) and Yonsei-KIST Convergence Research Program. The authors thank Lauren Plavisch for English language editing.

References

1 N. Q. Minh, *J. Am. Ceram. Soc.*, 1993, **76**, 563–588.
2 S. C. Singhal, *Solid State Ionics*, 2000, **135**, 305–313.
3 E. D. Wachsman and K. T. Lee, *Science*, 2011, **334**, 935–939.
4 R. A. George and N. F. Bessette, *J. Power Sources*, 1998, **71**, 131–137.
5 A. Khandkar and S. Elangovan, *Denki Kagaku*, 1990, **58**, 551–556.
6 S. de Souza, S. J. Visco and L. C. De Jonghe, *J. Electrochem. Soc.*, 1997, **144**, L35–L37.
7 J.-W. Kim, A. V. Virkar, K.-Z. Fung, K. Mehta and S. C. Singhal, *J. Electrochem. Soc.*, 1999, **146**, 69–78.
8 K. Sato, C. Iwata, N. Kannari and H. Abe, *J. Power Sources*, 2019, **414**, 502–508.
9 Y. Yamaguchi, I. Kagomiya, S. Minami, H. Shimada, H. Sumi, Y. Ogura and Y. Mizutani, *J. Power Sources*, 2020, **448**, 227426.
10 W. B. Guan, H. J. Zhai, L. Jin, T. S. Li and W. G. Wang, *Fuel Cells*, 2011, **11**, 445–450.

11 T. L. Wen, D. Wang, H. Y. Tu, M. Chen, Z. Lu, Z. Zhang, H. Nie and W. Huang, *Solid State Ionics*, 2002, **152–153**, 399–404.
12 H. Y. Jung, S. H. Choi, H. Kim, J. W. Son, J. Kim, H. W. Lee and J. H. Lee, *J. Power Sources*, 2006, **159**, 478–483.
13 S. P. Jiang, J. G. Love and L. Apateanu, *Solid State Ionics*, 2003, **160**, 15–26.
14 K. D. Seo, Y. J. Kim, J.-y. Park and H.-T. Lim, *Int. J. Hydrogen Energy*, 2018, **43**, 2349–2358.
15 R. Spotorno, P. Piccardo and G. Schiller, *J. Electrochem. Soc.*, 2016, **163**, F872–F876.
16 K. Föger, *ECS Proceedings Volumes*, 1999, **1999-19**, 95–100.
17 S. Sugita, Y. Yoshida, H. Orui, K. Nozawa, M. Arakawa and H. Arai, *J. Power Sources*, 2008, **185**, 932–936.
18 M. C. Tucker, L. Cheng and L. C. DeJonghe, *J. Power Sources*, 2011, **196**, 8435–8443.
19 N. Huang, B. Han, Y. Wang, Y. Li, Y. Su, W. Guan, X. Zhou, M. Chai and S. C. Singhal, *Int. J. Hydrogen Energy*, 2021, **46**, 20078–20086.
20 M. Shen and P. Zhang, *Int. J. Hydrogen Energy*, 2020, **45**, 33876–33894.
21 S. P. Simner, M. D. Anderson, L. R. Pederson and J. W. Stevenson, *J. Electrochem. Soc.*, 2005, **152**, A1851.
22 Y. T. Yu, J. H. Zhu and B. L. Bates, *Int. J. Hydrogen Energy*, 2020, **45**, 27745–27753.
23 X. Xin, L. Liu, Y. Liu and Q. Zhu, *Int. J. Hydrogen Energy*, 2018, **43**, 23036–23040.
24 E. N. Naumovich, K. Zakharchuk, S. Obrębowski and A. Yaremchenko, *Int. J. Hydrogen Energy*, 2017, **42**, 29443–29453.
25 M. C. Tucker, L. Cheng and L. C. DeJonghe, *J. Power Sources*, 2013, **224**, 174–179.
26 A. Morán-Ruiz, K. Vidal, A. Larrañaga, J. M. Porras-Vázquez, P. R. Slater and M. I. Arriortua, *Int. J. Hydrogen Energy*, 2015, **40**, 8407–8418.
27 A. Morán-Ruiz, K. Vidal, A. Larrañaga, J. M. Porras-Vázquez, P. R. Slater and M. I. Arriortua, *Int. J. Hydrogen Energy*, 2015, **40**, 4804–4818.
28 J. Will and L. J. Gauckler, *ECS Proceedings Volumes*, 1997, **1997-40**, 757–764.
29 R. E. Vandenberghe, G. G. Robbrect and V. A. M. Brabers, *Phys. Status Solidi A*, 1976, **34**, 583–592.
30 A. Petric and H. Ling, *J. Am. Ceram. Soc.*, 2007, **90**, 1515–1520.
31 R. Zhan, Y. Wang, M. Ni, G. Zhang, Q. Du and K. Jiao, *Int. J. Hydrogen Energy*, 2020, **45**, 6897–6911.
32 A. Mathur and J. Erlebacher, *Appl. Phys. Lett.*, 2007, **90**, 061910.
33 R. Liu and A. Antoniou, *Acta Mater.*, 2013, **61**, 2390–2402.
34 L. J. Gibson and M. F. Ashby, *Proc. R. Soc. London, Ser. A*, 1982, **382**, 43–59.
35 E. Buckingham, *Phys. Rev.*, 1914, **4**, 345–376.
36 D. Ansel, J. W. Liu, M. Bohn and J. Debuigne, *Oxid. Met.*, 1993, **39**, 31–54.
37 C. Yoon and D. L. Cocke, *Appl. Surf. Sci.*, 1988, **31**, 118–150.
38 K. Wandelt and G. Ertl, *Surf. Sci.*, 1976, **55**, 403–412.
39 S. P. Jiang, *J. Power Sources*, 2003, **124**, 390–402.
40 J. Pan, J. Yang, D. Yan, J. Pu, B. Chi and J. Li, *Int. J. Hydrogen Energy*, 2020, **45**, 17927–17934.
41 W.-J. Shong, C.-K. Liu, W.-H. Shiu and R.-Y. Lee, *Int. J. Hydrogen Energy*, 2019, **44**, 4317–4331.
42 J. Yang, D. Yan, W. Huang, J. Li, J. Pu, B. Chi and L. Jian, *Energy*, 2018, **149**, 903–913.